*Proceedings of the*
*Annual Stability Conference*
*Structural Stability Research Council*
*St. Louis, Missouri, April 2-5, 2019*

# Experimental and numerical investigation of local stability of flexural cold formed high strength steel hollow section profiles

Ieva Misiunaite[1], Ronaldas Jakubovskis[2], Aleksandr Sokolov[3], Arvydas Rimkus[4], Viktor Gribniak[5]

## Abstract

Cold-formed hollow sections are the leading tubular profiles used in structural design. High strength combined with stiff form of welded hollow section enables creation of robust and lightweight structures. Because of favorable ratio between load bearing capacity and weight, high strength steels (HSS) rapidly conquering the position in steel structures market as well as gaining the attention of researchers. Nominally HSS resistance to both, stress and strain, is doubled (considering the ordinary steel as the reference), though the elastic deformation range is remaining narrow. Analysis of nonlinear effects and slenderness of the internal parts of cross-section through the bending zone of the flexural member, demands for consideration of interaction between bending and local stability of the web. This paper presents an experimental and numerical analysis of deformation behavior of cold-formed hollow sections made of high strength steels, based on strain monitoring approach. In-plane bending tests, in four-point bending configurations, on HSS sections in grades S700MLH, S900MH were conducted. It was found that both grades HSS cross-sections, having the same aspect ratio, exhibit comparable global and local failure modes. The experimental results were simulated by means of non-linear finite element approach with the aim to develop validated numerical models to predict deformation behavior of HSS tubular profiles in flexure. Moreover, the innovative digital image correlation technique used for the nondestructive strain monitoring is presented and its advantageous applicability for the analysis of HSS profiles local deformation behavior is discussed using the obtained test results. Gathered experimental results and numerical simulation outputs were discussed to clarify non-linear effects characteristic of deformation behavior of the hollow section profiles. Particular attention was paid to the distinct deformation response at the loading points and the resemblance of the failure mode observed during the tests.

## 1. Introduction

Recent advances of technology in material science give the impression of a gradual tendency towards the structural utilization of high strength steels. More than three decades ago, steel with

[1] Postdoc Research Fellow, Vilnius Gediminas Technical University, <ieva.misiunaite@vgtu.lt>
[2] Senior Research Fellow, Vilnius Gediminas Technical University, <ronaldas.jakubuvskis@vgtu.lt>
[3] Senior Research Fellow, Vilnius Gediminas Technical University, <aleksandr.sokolov@vgtu.lt>
[4] Senior Research Fellow, Vilnius Gediminas Technical University, <arvydas.rimkus@vgtu.lt>
[5] Professor, Vilnius Gediminas Technical University, <viktor.gribniak@vgtu.lt>

a yield stress of 275 MPa was the standard, and steel of grade S355 the rarity. In those days, S355 serves as ordinary steel, and higher strength steels are offered by manufacture. The purpose for constantly growing use of high-strength steels (HSS) in structures is reasonable: a smaller amount of material, lower carbon emission, lighter supports and foundations, easer transportation and assembling.

High strength steels are used for bridge girders, particularly in trusses where self-weight is governing load (Miki 2002, Earls 2002, Wasserman 2003). For the flexural members in building structures the use of HSS commonly, is restricted by deflections. Thus, high strength steels can be applicable in trusses, commonly in short-span or heavily loaded ones for buildings like convention centres (Chen 2003, Lee 2017), or for long span structures, which usually are used for the roofs of arenas or stadiums and are designed under less strict serviceability limits because of large elevations. Additionally, self-weight of the structure is a significant proportion of the design load and thus a reduction in self-weight is valuable. Wherefore, there can be find successful practical applications of HSS used for long span roof trusses, the ones worth to mention would be: the retractable roof truss at the Reliant Stadium, Beijing's Bird's Nest Stadium, Sony Centre in Germany, Houston and the Airbus Hanger in Frankfurt Airport (Griffis 2003, Willms 2009). The main roof truss of Friends Arena in Stockholm uses S460, S690 and S900 steels in various structural forms for the chords and diagonals (Cederfeldt 2012).

Literature review showed that previous studies of HSS beams mainly focused on either built-up (Lee 2013) or hot-formed sections (Wang 2016), forming a gap in knowledge of structural behaviour of cold-formed sections. Cold-formed hollow sections are the leading tubular construction material. High strength in combination with naturally stiff shape of welded hollow section allows to construct robust and lightweight structures. On the other hand, cold-formed sections have specific problems related to their rounded corners and increased slenderness due to strength enhancement which may govern the resistance of the beam by the flange failure (crushing) as well as web crippling (local buckling). A limited number of studies has been carried out on the flexural behaviour of HSS cold-formed tubular beams and focused either on a pure bending resistance without respect to the local buckling (Ma 2016, Ma 2017) or the local buckling as governing bearing resistance singly (Li 2018). Hence, as part of a broader study on the structural behaviour of cold-formed HSS tubular sections the objective of this paper is to report on a failure mechanism and an analysis of the bearing resistance of cold-formed HSS square hollow sections (SHS) and to determine a methodology for accurately evaluating the deformation behaviour of the web and also providing an appropriate assessment of interaction for combined bending and local buckling.

The aim of the investigation was to obtain validated numerical models, through accurate replication of the test results which can serve as a reliable technique to determine combined bending and local buckling strength of the HSS square tubular beams. An experimental programme on the grades S700 and S900 SHS profiles was carried out at the Laboratory of Innovative Building Structures of Vilnius Gediminas Technical University. The program consisted of material tests and in-plain bending tests on a total of four SHS specimens loaded in four-points bending configuration up to a failure load. The deformation behaviour of the web was tracked using non-destructive digital image correlation (DIC) method to monitor the evolution of the strains. A numerical modelling study was carried out in parallel with the experimental program.

## 2. Experimental study

This section covers the experimental investigation of the bending moment resistance and deformation behavior of cold-formed high strength SHS beams, which was carried out through four-point bending tests. In four-point bending test the maximum flexural stress is distributed in the moment span complicating failure mode predictions. Thus, the four-point bending test was adopted with the aim to observe possible resemblance in the failure mode and enable more accurate predictions of the local deformation behavior of HSS tubular profiles. In total the experimental program encompasses four in-plane bending tests.

### *2.1 Material testing*

High strength steel elements were comprised of hot-rolled base materials, which were formed into quadratic shape and welded by high frequency inductive, longitudinal welding. The test SHS profiles embedded two high strength steel grades of S700 and S900. To measure the material properties of the considered structural profiles, flat tensile coupons were extracted from the sections and tested in a 100 kN capacity W + B testing machine. It should be noted that for each cross section two flat coupons were extracted from the flange (TF) opposite the weld and two from the web (TW) at 90 degrees angle from the welding seam. The dimensions of the flat coupons followed to the requirements of (EN ISO 6892-1 2016). Typical stress-strain curve of cold-formed steel sections has no yield plateau and exhibits insignificant strain hardening (Ma 2015, Wang 2017), thus 0.2% proof stress $\sigma_{0.2}$ is usually taken as the upper yield stress as shown in Fig. 1. Table 2 summarizes material test results. The material parameters presented in Table 2 are modulus of elasticity E, proof stress $\sigma_{0.2}$, the ultimate tensile stress $\sigma_u$, the strain $\varepsilon_{el}$ at the initial strain hardening which refers to the proportional limit yield stress $\sigma_{pL}$ as shown in Fig. 1, the strain $\varepsilon_{0.2}$ at the total yield stress $\sigma_{0.2}$, the ultimate tensile to yield stress ratio $\sigma_u/\sigma_{0.2}$, the percentage total extension at maximum force $A_{gt}$.

Table 1: Average tested material properties from tensile coupons.

| **Cross-section** | **Label** | **E (MPa)** | **$\sigma_{0.2}$ (MPa)** | **$\sigma_u$ (MPa)** | **$\varepsilon_{el}$ (mm/mm)** | **$\varepsilon_{0.2}$ (mm/mm)** | **$\sigma_u/\sigma_{0.2}$** | **$A_{gt}$ (%)** |
|---|---|---|---|---|---|---|---|---|
| **S700 80x80x3** | TF | 204731 | 768 | 828 | 3.75E-03 | 5.76E-03 | 1.08 | 1.49 |
| | TW | 213243 | 776 | 869 | 3.64E-03 | 5.64E-03 | 1.12 | 3.32 |
| **S900 100x100x4** | TF | 196492 | 1009 | 1101 | 5.13E-03 | 7.25E-03 | 1.09 | 1.94 |
| | TW | 208732 | 1018 | 1111 | 4.88E-03 | 6.88E-03 | 1.09 | 2.07 |

Fig. 1 shows the typical stress-strain curves of the flat coupons taken from the sections of the same grades and presents aforementioned stress and strain parameters which values are tabulated in Table 1. The grey zone in Fig. 1a and b identifies the elastic range of the material validated by the tensile modulus E and linear stress-strain relationship. Fig. 1 shows that steels S700 and S900 have high strength but lower ductility. The obtained material properties were used in the numerical simulations of the test specimens.

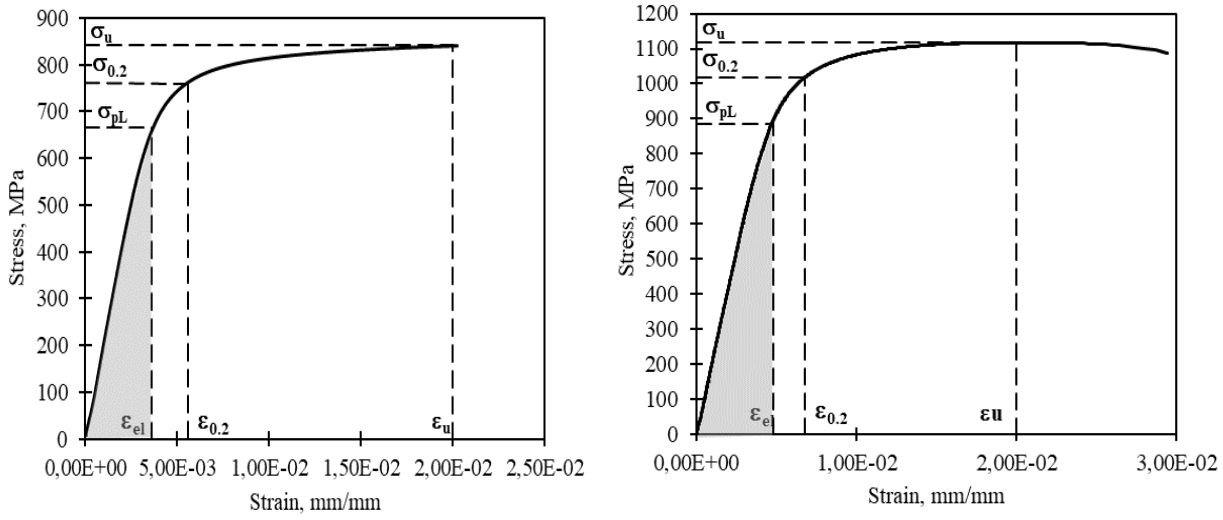


(a) S700 (b) S900

Figure 1: Measured stress-strain curves for tensile coupons

*2.2 Beam tests*

Four-points in-plane bending tests, with the same section geometry, but different steel grades, were conducted up to failure load to determine failure mode of the HSS beams and to assess their possible comparability to NSS. All specimens had a total length of 2200 mm, with equal overhangs at each end of 100 mm beyond the centerlines of the supports, which made the span of the beam equal to 2000 mm. Simple support conditions were reached by means of steel rollers and bearing plates, placed beneath the specimens, as shown in Fig. 2a. The test beams were loaded symmetrically using a 5000 kN hydraulic actuator in a stiff testing frame. The moment span by means of distance between spreader beam supports was 500 mm, thus making the length of the shear spans (750 mm) sufficient to guarantee that the section bending capacity would be reached before shear failures occurs (as shown in Fig. 2). The wooden pieces, with dimensions closely matching those of the steel specimens, were inserted within the tubes at the supports to avoid web crippling under the localized restoring loads. Contrarily, the beam sections beneath the loading points were left unreinforced in order to obtain local deformation behavior under simultaneous effect of bending and concentrated load. Linear variable displacement transducers (LVDT) located at a mid-span (LVDT3/4 with the range of 100 mm) and both loading points (LVDT1/2 and LVDT 5/6 with the range of 50 mm), were used to measure the vertical displacements in the moment span.

A load cell was used to measure the applied load. All results from the LVDT and the load cell were collected and recorded by an ALMEMO 2890-9 data logger. Strain measurement was performed using a high-speed camera and digital image correlation (DIC) system (as shown in Fig. 2b) with the aid of DaVis 8.1.6 software by Lavision. DIC is an innovative non-contact image analysis method, based on grey value digital images, that can determine the displacements of an object under load in three dimensions. The stereoscopic multi camera setup was used for measurements of 2D in-plane deformations with the capturing rate of 1 pic/kN (as shown in Fig. 2b). Local derivative calculations of the software give the strain tensors across the entire painted

surface of the specimen and enables to place a virtual strain gauge anywhere on the monitoring surface after the test, giving an accurate strain data.

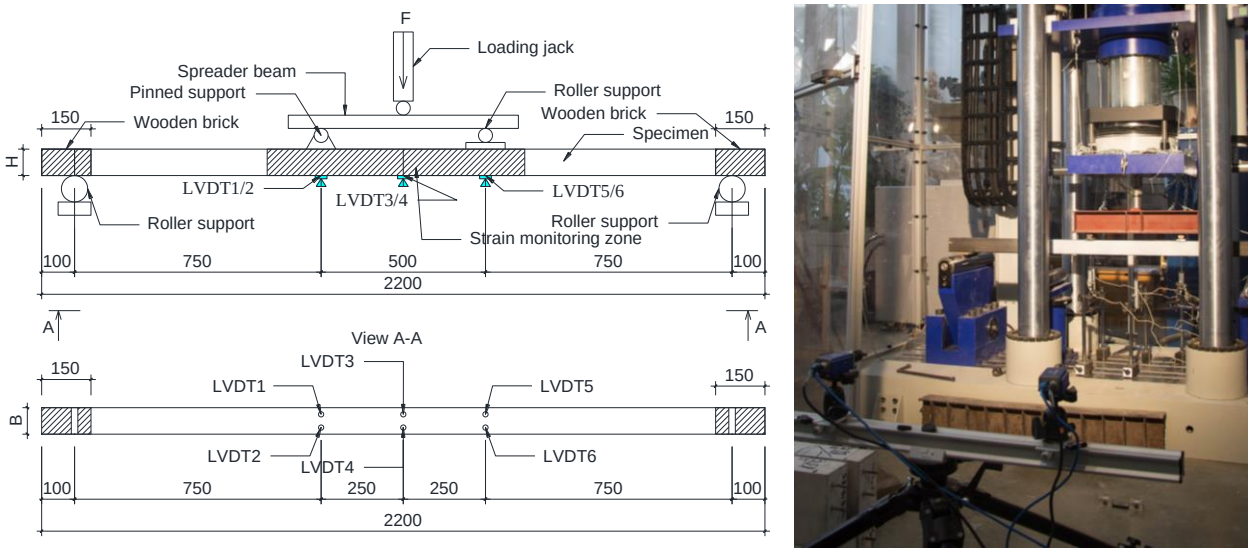


(a) Experimental arrangement (b) Strain monitorig

Figure 2: Experimental set-up of beam under four-point bending

Each specimen of steel was assigned a serial number denoted by "steel grade, referring to the nominal yield stress, section type and testing sequence". This study considers two types of SHS. According to their nominal dimensions they were abbreviated as follows: 8-type (80x80x3) and 10-type (100x100x4). Thus, the tests of HSS comprised the specimens: "S700-8-1", „S700-8-2", „S900-10-3", „S900-10-4". Table 2 presents the average measured geometric dimensions of the beams: B is the section width, H is the section depth, t is the thickness and r is the outer radius of the corner. The calculated elastic section modulus Wel, and plastic section modulus Wpl, the length of shear span Ls as well as the length of moment span Lm are arranged in the last four columns of the Table 2.

Table 2: Average measured dimensions for the specimens.

| Specimen | B (mm) | H (mm) | t (mm) | r (mm) | $W_{el}$ ($x10^3$mm) | $W_{pl}$ ($x10^3$mm) | $L_m$ (mm) | $L_s$ (mm) |
|---|---|---|---|---|---|---|---|---|
| S700-8-1 | 81.33 | 81.16 | 2.95 | 5.91 | 22.47 | 26.81 | 500 | 750 |
| S700-8-2 | 81.31 | 81.46 | 2.96 | 5.93 | 22.54 | 27.03 | 500 | 750 |
| S900-10-3 | 101.74 | 101.60 | 3.99 | 7.98 | 46.81 | 56.33 | 500 | 750 |
| S900-10-4 | 101.65 | 101.68 | 4.00 | 8.00 | 46.93 | 56.53 | 500 | 750 |

Table 3 shows the key test parameters of beams resistance, including the ultimate bending moment $M_u$ and corresponding curvature $\kappa_u$. The calculated cross-section elastic $M_{el}$ and plastic $M_{pl}$ moment capacities, obtained as the outcome of measured material yield strength $\sigma_{0.2}$, presented in Table 1, and the associated section modulus ($W_{el}$ or $W_{pl}$) based on the measured geometry from Table 2 together with the local slenderness of the flange $\lambda_f$ based on the material and geometric test properties given in Tables 1 an 2, respectively, are also presented in Table 3. The last column of the Table 3 summarizes the cross-section rotation capacity R. For the

sections, which failed to reach the plastic moment $M_{pl}$ capacity, the rotation capacity is assumed to be equal to zero (R=0).

Table 3: Summary of results from the bending tests

| Specimen | $\lambda_f$ | $M_u$ (kNm) | $\kappa_u$ x$10^{-4}$ ($mm^{-1}$) | $M_{el}$ (kNm) | $M_{pl}$ (kNm) | $M_u/M_{el}$ | $M_u/M_{pl}$ | R |
|---|---|---|---|---|---|---|---|---|
| S700-8-1 | 1.48 | 17.71 | 1.18 | 17.35 | 20.71 | 1.02 | 0.86 | 0.00 |
| S700-8-2 | 1.40 | 18.65 | 1.20 | 17.41 | 20.88 | 1.07 | 0.89 | 0.00 |
| S900-10-3 | 1.63 | 43.05 | 1.20 | 47.44 | 57.08 | 0.91 | 0.75 | 0.00 |
| S900-10-4 | 1.67 | 43.13 | 1.19 | 47.56 | 57.29 | 0.91 | 0.75 | 0.00 |

All tests specimens tend to fail earlier than attaining the plastic moment capacity. The slenderer sections experienced greater susceptibility to local buckling and therefore lower normalized moment capacity. The lower steel grade S700 specimens were capable to reach elastic moment capacity, while both S900 profiles failed before attaining elastic moment. Insignificat differences in the ultimate curvature of all test profiles refer to the lower ductility of the higher strength sections.

Fig. 3 illustrates typical failure of all test beams. It was observed that all the specimens tend to experience yielding and asymmetric local buckling of the compression flange and the compressive part of the web at the section under the roller support of the spreader beam, as presented in Fig. 3. The distinct deformation response at the loading points of HSS beams under four-point bending is discussed in Section 4.2.

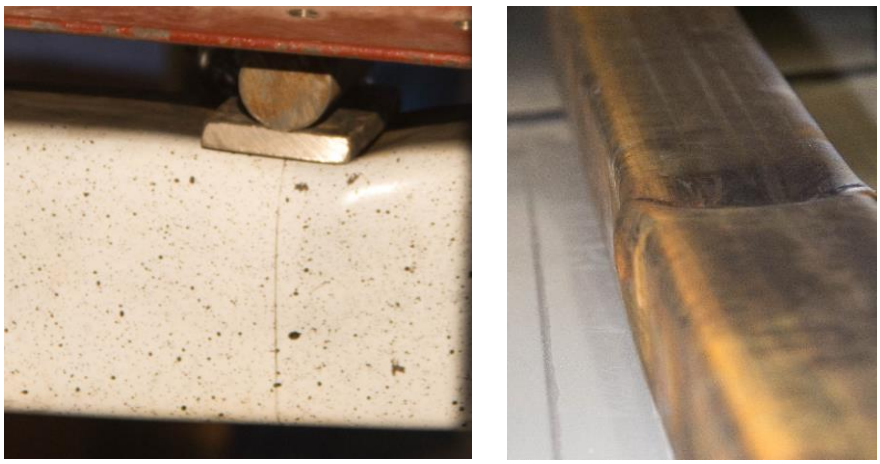

(a) Local failure of S900-10-3 (b) Local failure of S700-8- 2

Figure 3: Typical failure mode of the test beams

## 3. Numerical modeling

The numerical study was performed in two attempts. For the first attempt, adequacy of the numerical model was verified using the vertical displacements of the profiles and the local failure mode observed during the tests. Specimen S700-8-2 was chosen as a representative to verify the numerical model. The numerical analysis employed general purpose finite element (FE) software ANSYS. Parameters of the model were tailored seeking adequately represent

vertical displacements and particularly local failure of the profiles observed experimentally. A higher order 3-D solid elements, which exhibit quadratic displacement behavior were used. These elements are defined by 20 nodes having three degrees of freedom per node. The elements support plasticity, stress stiffening, large deflection, and large strain capabilities. A regular mesh with the average size of 20 mm was used. Experimental tests showed asymmetric local failure at the roller support of the spreader beam as identified in Fig. 2. In order to simulate the failure mode observed during the tests, the refined mesh was used for the region of the beam beneath the left loading point as shown in Fig. 5. A mesh convergence study was carried out to establish a sufficiently refined mesh size and an element size of 5 mm was found to be suitable to capture the local failure mode as shown in Fig. 5. As stated in EN 1993-5 Annex C (EN 1993-5 2006) the nominal geometric properties were incorporate in FE model. The boundary conditions were carefully selected to simulate the experimental set-up. At one end of the bottom flange all the displacements were restrained, while at the other end vertical and lateral displacements were restrained and the longitudinal was left free. The loading conditions were simulated as the pressure loads through the bearing plates replicating supports of the spreader beam shown in Fig. 2. The load was applied incrementally with 1 kN load step. The measured material stress-strain curves shown in Fig. 1 were employed in the development of the FE model. For the Ansys-Model the multilinear stress-strains curves were inputted in the form of true stress-strain response as recommended in EN 1993-5 Annex C (EN 1993-5 2006).

Validation of the model was based on the comparison of the obtained load-displacement response presented in Fig. 4 and the local failure shown in Fig. 5, which replicates the experimental failure given in Fig. 2.

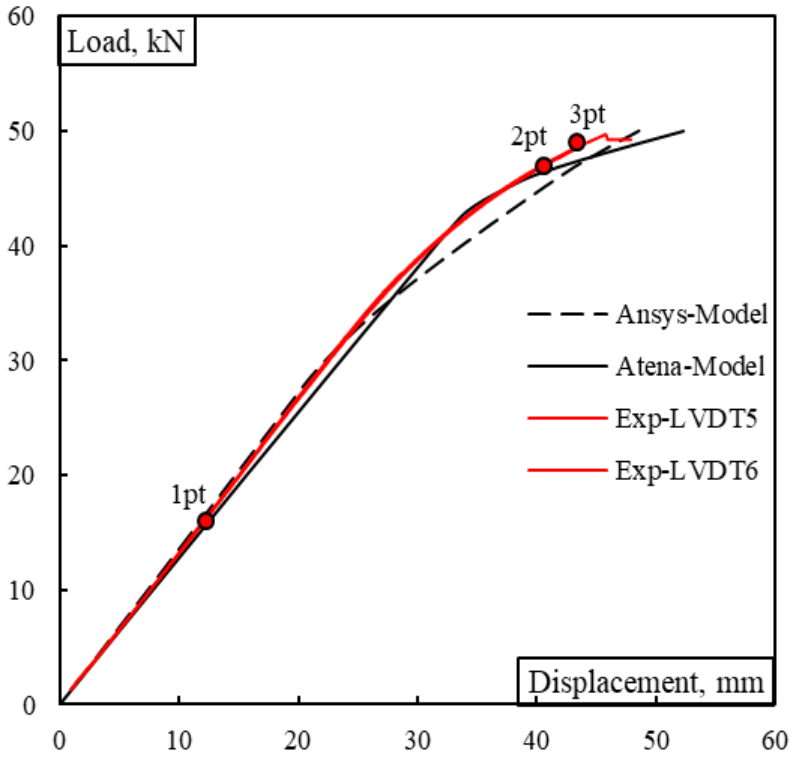

Figure 4: Experimental and numerical load-displacement response

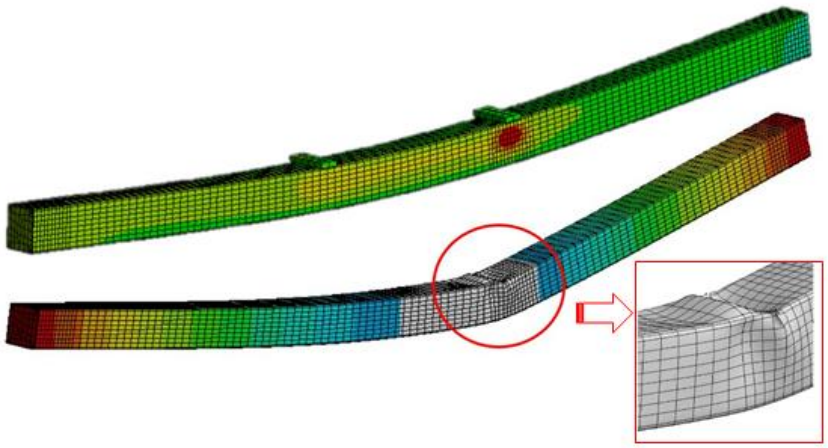

Figure 5: Numerical failure mode

Seeking for the modelling convenience and to decrease computational time, the simplified FE model was created using commercial FE software Atena. Non-linear isoparametric shell-solid elements with nine integration points in shell plane were used. In these elements six internal layers are distributed in the shell plane of the FE. 3D solid elements were used for the solid steel plates at the supports and point loads to avoid stress concentrations. Previously described general mesh size was used with the refinement of 5 mm at the loading point and resulted in the total number of finite elements equal to 4572, which is more than twice less than used in ANSIS-Model. The "von Mises with Hardening" material model using a bilinear curve for the calculation of stress values was incorporated in Atena-Model. For the elastic stress-strain region the approximated tensile modulus and yielding strength values were used. The plastic region of stress-strain had a slope equal to the strain hardening modulus H = 20 GPa, which was adjusted to the test results. The point load was applied incrementally: 4 kN load step was used in the range of elastic deformation, whereas load increment was reduced to 1 kN after the plastic deformations occurred.

Validation of the Atena-Model was based on the comparison of the obtained load-displacement response and resulted in a very good agreement as shown in Fig. 4. For the suitability to simulate local nonlinear-effects, Atena-model was validated using virtual strain measurements obtained by DIC method. The measurement of the strain was performed at the vicinity of the loading point where the local failure occurred with the distance of 10 mm from the bearing plate as shown in Fig. 6a. To obtain deformation response the 20 mm length numerical strain gauges were used and placed with the 10 mm distance through the flat range of the profile web. The same length and placement steps were used for the optical strain gauges to generate strain distribution from DIC results.

Fig. 6 presents the comparison of numerical and test strain distribution at the arbitrary loading points shown in Fig. 4. The grey color region in Fig. 6b distinguishes the elastic strain distribution and is limited to the approximate value of the proportional limit strain $\varepsilon_{el}$ obtained during material tests as shown in Fig. 1. The red color region corresponds to the plastic strains limited by the material tests strain $\varepsilon_{0.2}$ at the total yield stress $\sigma_{0.2}$ as indicated in Fig. 1. The comparison of strain distribution from the test and Atena-Model shown in Fig. 6b presents accurate replication of the deformation behavior in both elastic and plastic strain regions. Although, the FE Atena-Model could not accurately simulate high plastic deformation at the

vicinity of web and flange junction at 3 pt corresponding to failure load, the visual shift of the center of gravity (CG) to position CG' serves as indication to the local buckling failure.

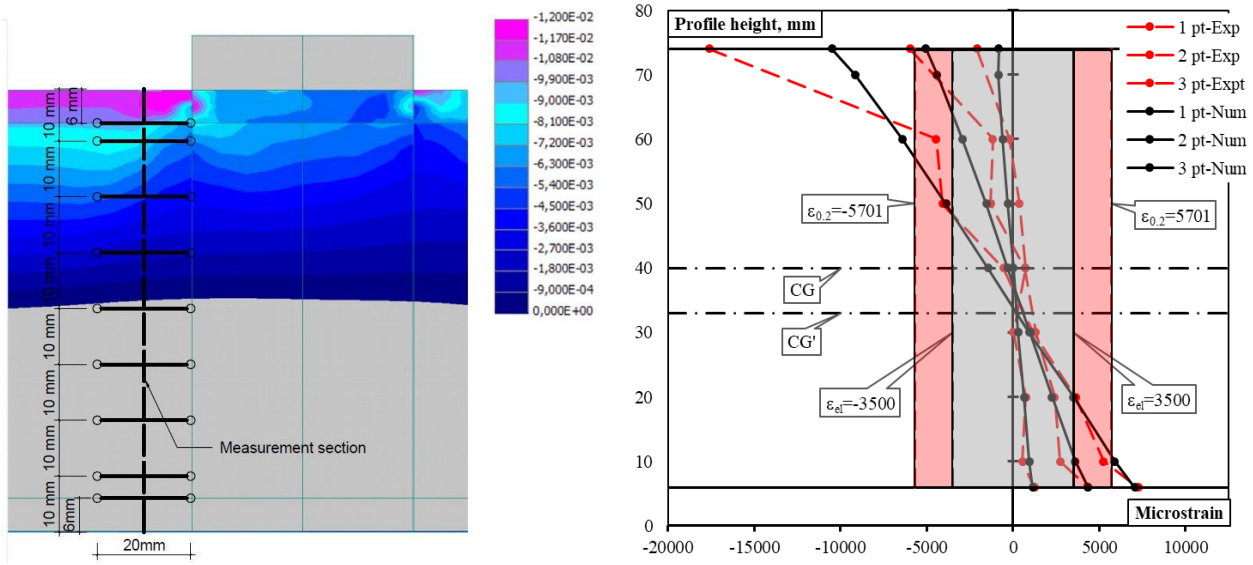


(a) Set-up of the numerical strain gauges (b) Comparison of strain distribution

Figure 6: Experimental and numerical strain measurement results

Fig. 4 - Fig. 6 show that both FE models closely predict load-displacement response and the beam failure modes. The less computation time of Atena-Model comparing to Ansys-Model makes it more convenient for the HSS profiles numerical data generation.

## 4. Discussion of the results

In this section, the gathered experimental results and numerical simulation outputs are discussed to clarify non-linear effects characteristic of deformation behavior of the SHS profiles. Particular attention is paid to the distinct deformation response at the loading points and the local buckling observed during the tests. The advantages of applicability of the innovative DIC strain monitoring technique for the analysis of HSS profiles local deformation behavior is discussed using the obtained test results.

### *4.1 Bending moment resistance*

Fig. 3 shows that all the test specimens tend to experience similar failure mode, which appeared in the moment span at the point load by means of the roller support of the spreader beam (see Fig. 2). The asymmetric non-simultaneous local failure of the tubes was determined due to the force concentration introduced by the rotation of the spreader beam roller support. Fig. 7 illustrates the moment-curvature response at both loading points of the considered HSS profiles. For all the tests the same set-up presented in Fig. 2 was used. Thus, for the convenience purposes hereafter pin and rollers supports of the spreader beam will be identified as the left and right loading points, respectively.

The curvature $\kappa_{Ls}$ at the loading points in the distance equal to the shear span $L_s$ (as shown in Table 2) was obtained using the results from the displacement transducers and can be calculated

using the expression in Eq. (1), where $\delta_{Ls}$ is the vertical displacement at the loading point obtained as an outcome of LVDT1/2 or LVDT5/6 (as shown in Fig. 2) measurements, Ls and $L_m$ are the shear and moment span, respectively as presented in Fig.2.

$$\kappa_{Ls} = \frac{6\delta_{Ls}}{2L_s^{\,2} + 3L_s L_m} \tag{1}$$

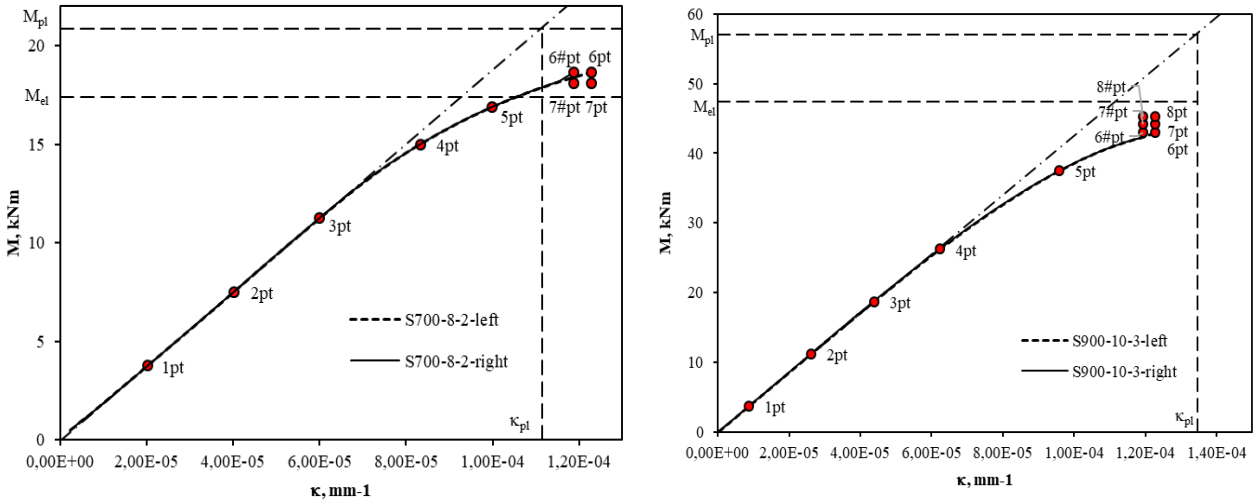


(a) Specimen S700-8-2 (b) Specimen S900-10-3

Figure 7: Moment-curvature response of the high strength steels

The moment-curvature response and deformed behavior of the specimens S700-8-2 and S900-10-3 were chosen as the representatives for the discussion of the results. Considering the moment-curvature response of both beams presented in Fig.7, no significant deference can be observed between the left and right loading points results. Due to the local buckling, HSS beams exhibits slightly lower values of the curvature at right side loading point in comparison to the left side results. Comparing moment-curvature response between different steels it can be observed, that specimen S700-8-2 experience linear behavior in the range limited by the moment equal to approximately two thirds of the ultimate moment, while the specimen S900-10-3 tends to behave linear just till half of the ultimate moment. Due to higher susceptibility to nonlinearities the moment capacity of the specimen S900-10-3 was limited by the local buckling of the cross-section.

*4.2 Results of strain monitoring*

Fig. 8 shows strains distribution of the S700-8-2 specimens at the arbitrary loading steps, monitored using DIC technique. The strains were measured at the vicinity of the loading points by means of virtual strain gauges positioned as described in Section 3 and presented in Fig. 6a. Local deformation behavior of the web is plotted through the height (flat part of the web) of the profile. The arbitrary loading points are denoted in Fig. 7a. The grey color region in Figs. 8 and 9 distinguishes the elastic strain distribution and is limited to the approximate value of the proportional limit strain $\varepsilon_{el}$ obtained during material tests as shown in Fig. 1. The red color region in Fig. 8 corresponds to the plastic strains limited by the material tests strain $\varepsilon_{0.2}$ at the total yield stress $\sigma_{0.2}$ as indicated in Fig. 1. The linear trendlines were used to capture the varying

position of the center of gravity (CG). From the results presented in Fig. 7 the distinct deformation behavior at the left and right loading points can be observed. The strain distribution and constant position of the CG shown in Fig. 7a identifies that web is subjected to bending with no evident compression until the ultimate load (6 pt) is reached. The contrary situation can be observed in Fig. 7b. The CG of the section shifts to the position CG' at relatively low loading level (4 pt) and the strains at exceed elastic region. This refers to partial yielding of the flange followed by stress concentration and web subjected to bending and compression. The shifted centroid CG' remains at the same position until the ultimate load is reached (6#pt). Remaining position of the shifted centroid of gross cross-section CG' at the ultimate load identifies that the sections can resist partial yielding of the compressive parts at the level ($\varepsilon_{0.2}$) required for a fully elastic stress distribution. Thus, the shifted centroid CG' can be considered as pseudo-elastic neutral axis of the cross-section of reduced height. Failure of the section was caused by the local buckling which can be distinguished by significant shift of CG, presented by trendline (7#pt) with high plastic deformations at the vicinity of web-to-flange junction, which are close to the ultimate strain ($\varepsilon_u$) obtained by material tests as shown in Fig. 1. Although, the deformations at the left section (Fig. 7a) at the same loading point exceed the limit of plastic strain ($\varepsilon_{0.2}$), they remain at the relatively low level of the plastic strains in comparison to results presented in Fig. 7b.

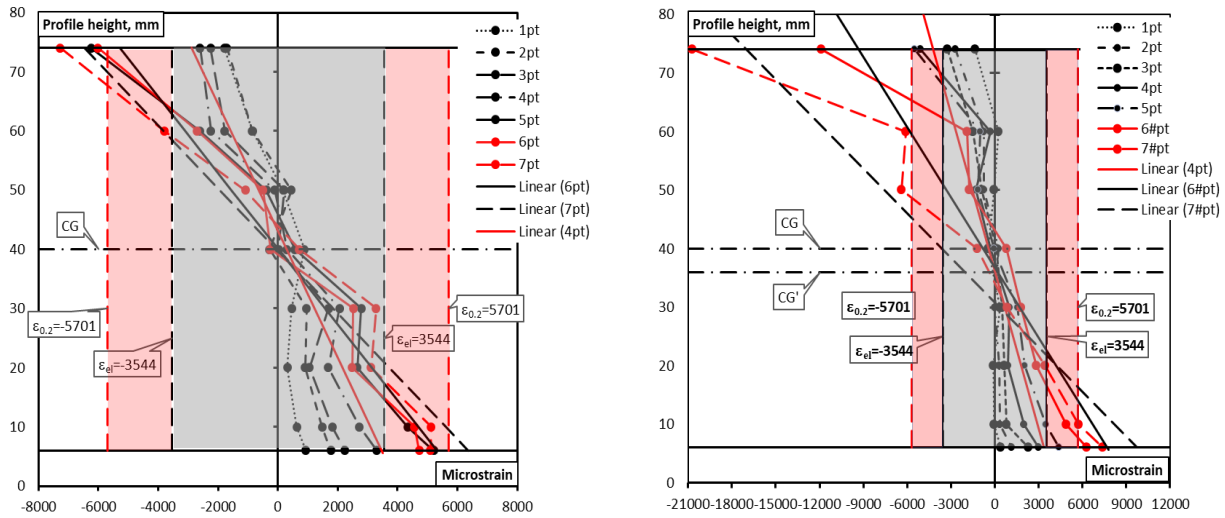


(a) Left side (b) Right side

Figure 8: Strain maps of the specimen S700-8-2

Quite specific strain distribution was observed during the test of the profile made of steel S900. Fig. 9 shows the shift of CG to the position CG' at relatively low loading level (3 pt) identifying the significant influence of the premature nonlinear effects. As can be observed in Fig. 9b, the deformations are mainly localized in the outer layers of the section. Such localization is characteristic until the loading 6#pt, denoted in Fig. 7b. That indicates governing local buckling effects and suitability of the theoretical models for the analysis of slender sections proposed by most of design codes, which deny inefficient part of the section for estimating the load bearing capacity of the slender sections. As expected, local buckling corresponding to the strains below the yield plateau has caused failure of the section. Fig. 9 demonstrates that the ultimate tensile

strains in the outer layers of the section do not exceed the elastic limit $\varepsilon_{el}$ almost until failure of the section.

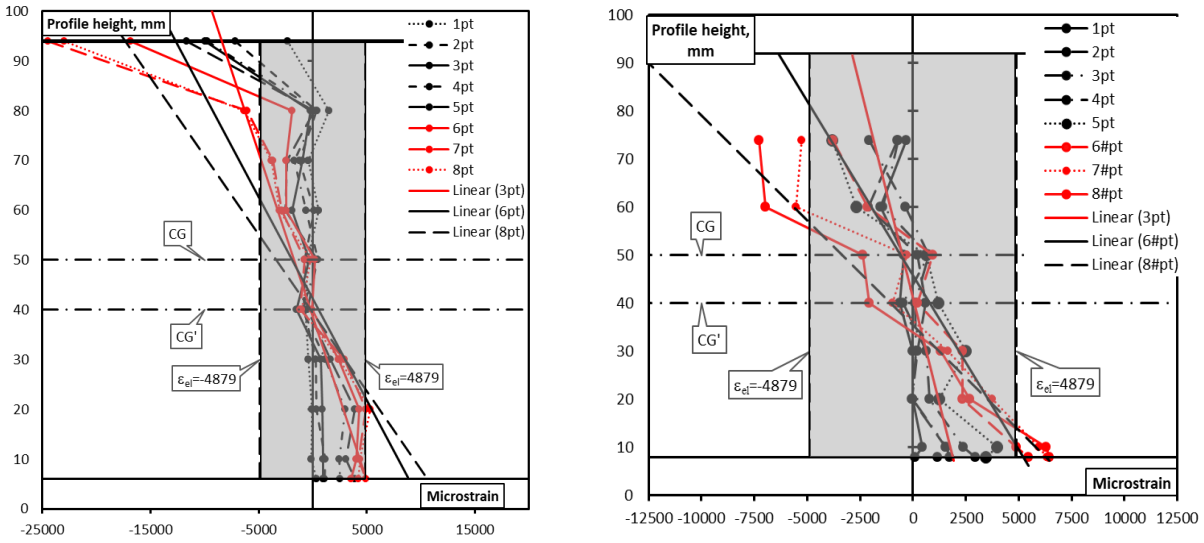


(a) Left side (b) Right side

Figure 9: Strain maps of the specimen S900-10-3

Deformation behavior presented in Figs. 8 and 8 well agree with the moment-curvature response shown in Fig. 6. By comparing these test outcomes, the following comments could be drawn:

- S700-8-2. The sections can resist partial yielding of the compressive parts at the level ($\varepsilon_{0.2}$) required for a fully elastic stress distribution and the beams are capable to attain the elastic moment resistance. The load concentration is seen to have significantly high influence on the local failure of the beams.
- S900-10-3. The sections are highly susceptible to nonlinear effects and the beams fail before reaching elastic moment capacity. Their deformation behavior reflects the theoretical models for slender sections resistance evaluation provided by the design codes.

## 4. Conclusions

The experimental program comprising four in-plane bending tests, in four-point bending configuration on cold-formed high strength steel profiles was described in this paper. Two different geometries of square hollow sections (80x80x3 and 100x100x4) were examined with two different series of high strength steel grades of 700MPa and 900MPa. The moment-curvature response and deformation behavior have been evaluated. Based on the tests carried out for this study, the following conclusions have been drawn:

- Asymmetric local buckling caused failure of all specimens. The nonlinear effects as well as an interaction of bending and local buckling of the web for cold-formed HSS sections can be accurately evaluated using digital image correlation technique.
- The combined bending and local buckling resistance of cold-formed HSS sections can be determined using numerical models, validated against test results obtained with applied monitoring system composed of devices for monitoring global (vertical displacements)

and local effects (instability/buckling). Suggested numerical models can serve as a suitable methodology for the design of HSS tubular sections.


## Acknowledgments

The research leading to these results has received funding from the Lithuanian Research Council under grant agreement No. 09.3.3-LMT-K-712-02-0159.


## References


Miki, C., Homma, K., Tominaga, T. (2002). "High strength and high performance steels and their use in bridge structures." *Journal of Constructional Steel Research*, 58(1) 3-20.

Earls, C.J., Shah, B.J. (2002). "High performance steel bridge girder compactness." *Journal of Constructional Steel Research*, 58(5-8) 859-880.

Wasserman, E.P., Pate, W.H., Huff, T. (2003). "The evolution of best practices with high performance steel for bridges." *Proceedings of Advanced Materials for Construction of Bridges, Buildings, and Other Structures III*, Art. 10.

Chen, K., Axmann, G. (2003). "Comprehensive design and A913 grade 65 steel shapes: the key design factors of 300 Madison Avenue, New Your City." *Proceedings of North American Steel Construction Conference (NASCC)*, Baltimore, Maryland.

Lee, C-H. (2017). "Structural performance of 800 MPa high-strength steel members and application to high-rise and mega building structures." *International Journal of High-Rise Buildings*, 6(3) 249-259.

Griffis, L. (2003). "Comprehensive design and A913 grade 65 steel shapes: the high strength steel in the long-span retractable roof of Reliant Stadium." *Proceedings of North American Steel Construction Conference (NASCC)*, Baltimore, Maryland.

Willms, R. (2009). "High strength steel for steel constructions." *Proceedings of Nordic Steel Construction Conference (NSCC 2009)*, Malmo, Sweden. 597-604.

Cederfeldt, J., Sperle, J-O. (2012). "Environmental advantages of using advanced high strength steel in steel constructions." *Proceedings of Nordic Steel Construction Conference*, Oslo, Norway.

Lee, C.H., Han, K.H., Uang, C.M., Kim, D.K., Park, C.H., Kim, J.H. (2013). "Flexural strength and rotation capacity of I shaped beams fabricated from800-MPa steel." *Journal of Structural Engineering ASCE*, 139 (6) 1043–1058.

Wang, J., Afshan, S., Gkantou, M., Theofanous, M., Baniotopoulos, C., Gardner, L. (2016). "Flexural behaviour of hot-finished high strength steel square and rectangular hollow sections." *Journal of Constructional Steel Research*, 121(2016) 97–109.

Ma, J-L., Chan, T-M., Young, B. (2016). "Experimental investigation of cold-formed high strength steel tubular beams". *Engineering Structures*, 126 (2016) 200-209.

Ma, J-L., Chan, T-M., Young, B. (2017). "Design of cold-formed high strength steel tubular beams." *Engineering Structures*, 151 (2017) 432-443.

Li, H-T., Young, B. (2018). "Design of cold-formed high strength steel tubular sections undergoing web crippling." *Thin-Walled Structures* ,133 (2018) 192-205.

EN ISO 6892-1: 2016, Metallic material – Tensile testing – Part 1: Method of test at room temperature, International Organization for Standardization, 2016.

Ma, J-L., Chan, T-M., Young, B. (2015). "Material properties and residual stresses of cold-formed high strength steel hollow sections." *Journal of Constructional Steel Research*, 109(2015) 152-165.

Wang, J., Afshan, S., Schillo, N., Theofanous, M., Feldmann, M., Gradber. L. (2017). "Material properties and compressive local buckling response of high strength steel square and rectangular hollow sections." *Engineering Structures*, 130(2017) 297-315.

EN 1993-1-5, Eurocode 3: design of steel structures. Part 1–15: Plated structural elements, *European Committee for Standardization*, Brussels, Belgium: (CEN), 2006.